Boundary-Layer Meteorol
DOI 10.1007/s10546-010-9506-z

ARTICLE

Wind-Speed Undulations Over Swell: Field Experiment and Interpretation

Y. P. Soloviev · V. N. Kudryavtsev

Received: 14 July 2009 / Accepted: 4 May 2010

Abstract Results of field measurements of the swell-induced undulation of the wind speed taken from a Black Sea platform are presented. The wind speed and its fluctuations were measured at several heights between 1.3 and 21 m above the mean sea level under various wind and swell conditions. Parameters of the swell-induced undulations were derived from cross spectra of the wind-speed fluctuations and the sea-surface displacement. As found, the phase and the amplitude of the wind speed undulation in the layer from $k_p z = 0.1$ to $k_p z = 3$ (k_p is the swell wavenumber) are in good agreement with the theory of inviscid shear flow over a wavy surface. The main feature of the vertical profile of the swell-induced undulation is the exponential attenuation of its amplitude with height typical for the potential flow over the fast running waves. At the lowest levels the potential undulations are significantly distorted by the wind-speed variations caused by the vertical displacements of the shear airflow relative to a fixed sensor. No direct impact of swell on the mean properties of the turbulent boundary layer at $k_p z > 0.1$ is revealed. In particular, the mean wind-speed profile and spectra of the horizontal velocity in the inertial subrange obey Monin-Obukhov similarity theory.

Keywords Air flow · Surface waves · Swell-induced velocity · Turbulence · Wind-speed profile

Y. P. Soloviev (✉) · V. N. Kudryavtsev
Marine Hydrophysical Institute, Sebastopol, Ukraine
e-mail: yuri_soloviev@mail.ru

V. N. Kudryavtsev
Nansen International Environmental and Remote Sensing Center, St. Petersburg, Russia

V. N. Kudryavtsev
Russian State Hydrometeorological University, St. Petersburg, Russia

Published online: 25 May 2010

1 Introduction

It is widely accepted that swell can significantly affect the sea-surface drag and the dynamics of the turbulent atmospheric boundary layer. Donelan et al. (1997) and Drennan et al. (1999) were the first to find a strong increase in the drag coefficient at low winds in the presence of swell travelling across or opposite to the wind. Later Guo-Larsen et al. (2003) and Pan et al. (2005) showed that the magnitude of the surface drag increases with an increase in the angle of swell propagation with respect to the wind direction. Low winds and the presence of swell are typical of tropical ocean regions, where the atmosphere accumulates heat and moisture and then transports these to higher latitudes. In this respect understanding of swell impact on exchange processes at the air–sea interface is one of the key issues the climate research.

Swell travelling faster than the wind transfers momentum to the atmospheric boundary layer. Depending on the swell direction the swell-induced momentum flux can accelerate (as for a following-wind swell) or decelerate (as for an opposite-wind swell) the airflow (e.g., Volkov 1970; Davidson and Frank 1973; Smedman et al. 1999; Drennan et al. 1999; Grachev and Fairall 2001), or may result in the rotation of the wind-stress vector (Geernaert et al. 1993; Rieder et al. 1994; Grachev et al. 2003). The formation of the wave-driven wind in a laboratory tank was first reported by Harris (1966), and the experimental evidence of this effect in real conditions was later reported by Miller (1999), Smedman et al. (1999) and Rutgersson et al. (2001).

Kudryavtsev and Makin (2004) proposed a physical model describing the impact of fast-running swell on the surface drag and the wind-velocity profile due to the pumping of swell momentum to the marine atmospheric boundary layer (MABL). The model is based on the two-layer approximation of the boundary layer: the near-surface inner region, where the swell-induced momentum and the energy fluxes are confined, and the outer region above. The model was able to reproduce quantitatively the main experimental findings, viz. the impact of ocean swell on the sea-surface drag and the formation of swell-driven wind. However, as mentioned by these authors, this consistency was achieved by an "artificial" enhancement of the swell attenuation rate, which in turn resulted in too fast a decay of swell on scales of about 1000 km. This scale is significantly less than the decay scale recently reported by Ardhuin et al. (2009) on the basis of global observations of ocean swell from satellite radar, 2700 km for the steep ocean swell and 20,000 km for swell of small steepness. Kudryavtsev and Makin (2004) amplified the swell attenuation rate in order to compensate for too small a depth of the inner region l (l is of order $kl \propto 10^{-2}$, where k is the swell wavenumber), which was conceptually based on rapid distortion theory (Belcher and Hunt 1993). Hanley and Belcher (2008), following in general line the model approach suggested by Kudryavtsev and Makin (2004), defined the inner region depth as $kl \approx 0.1$, and found a qualitative consistency between the model and observed swell-driven wind. Sullivan et al. (2008) performed large-eddy simulations (LES) of the impact of swell on the MABL and compared their results with measurements from the CBLAST field campaign (Edson et al. 2007). They found that the depth of the layer directly affected by swell is about $kl \propto 1$, i.e. it is much deeper than predicted by rapid distortion theory.

All these effects result from the averaged impact of the swell-induced undulation on the mean turbulent flow. In this context, experimental data of the vertical profiles of the amplitude and phase of the wind velocity, pressure and the turbulent stress undulation could identify the physical mechanism that leads to the averaged impact of swell on MABL dynamics. However, field measurements of the wave-induced undulation of the airflow are very limited. Earliest observations were reported at the end of the 1960s and beginning of the 1970s (e.g. Volkov 1969; Yefimov and Sizov 1969; Kondo et al. 1972). Kondo et al. (1972) presented

profile measurements of the mean wind speed and its undulation caused by mixed seas. They did not found any systematical deviation of the wind profile from the log shape, but revealed some discrepancies between the observed wave-induced undulation in wind speed and the model predictions based on Miles' theory (1957). However, Hristov et al. (2003) found that the amplitude and phase of the wind-velocity undulation are in agreement with the quasi-laminar Miles' (1957) theory. They came to the conclusion that the observed features of the wind-velocity undulation may serve as experimental evidence that the mechanism of the wind-wave generation proposed by Miles (1957) is efficient in open ocean conditions. Mastenbroek et al. (1996), using a two-dimensional (2D) numerical model for the atmospheric boundary layer based on the second-order closure scheme for the Reynolds stress, performed simulations of the wave-induced undulation of the turbulent airflow and its mean quantities (wind and turbulent stress profiles) measured in the large IRPHE-Luminy wind-wave tank. A good quantitative agreement between measurements and the model for the amplitude and phase of the wave-induced undulation was found. Also Mastenbroek et al. (1996) provided the experimental evidence for the validity of the rapid distortion theory: they revealed the existence of the inner region (where the wave-induced momentum flux is confined) and the outer region, where the wave-induced motion is almost inviscid. Hsu and Hsu (1983) studied the wind profile and the turbulent stress above waves in laboratory conditions, and analysis of their data by Kudryavtsev et al. (2001) also confirmed the existence of the inner region as a layer where the undulation of the turbulent stress is confined.

In our study we present results of field measurements of the swell-induced undulation in the wind speed taken from a Black Sea platform at several levels above the sea surface. The main goal is to investigate the vertical profile of the amplitude and phase of the wind-speed undulation and to compare these results with model predictions. We anticipate that these data will contribute to a better understanding of MABL dynamics above fast-running waves and facilitate improvements of models of swell decay and swell impact on the sea-surface drag.

2 Field Experiment

The experiment was carried out during September–October 2003 and September 2005 in the Black Sea coastal zone using the Marine Hydrophysical Institute's research platform located 700 m offshore at 30-m depth (see Fig. 1). Measurements of the wind speed and its fluctuations were performed using fast-response cup anemometers (the distance constant is 0.3 m) that gave wind-speed fluctuations with a frequency response of 1–4.5 Hz. Cup anemometers were fixed on a vertical mast mounted at the end of 9-m long beam and located at five to seven heights inside the 1.3–8 m layer above mean sea level. The altitudes of anemometers were changed depending upon wave height, measured with a wire resistant wave gauge mounted beneath the anemometers. The typical length of the wind speed and wave records was about 40–60 min with sampling rates of 0.1 or 0.2 s. An additional cup anemometer and a small vane for the registration of wind direction were mounted at 20.8 m height on a mast at the platform's corner. The accuracy of the wind-speed measurements using cup anemometers (established in the wind tunnel) is about 2%, and the relative error of the wind-speed measurements was investigated in a number of calibration tests. During these tests measurements of the wind speed were made using all of the anemometers fixed at the same level. In the range of wind speeds from 2 to 12 m s^{-1} the error in measurements of the mean wind speed and the variance of the velocity fluctuations was within ± 2 and $\pm 5\%$ respectively. The distortion of the oncoming airflow by the platform in the vicinity of the wind-speed measurements,

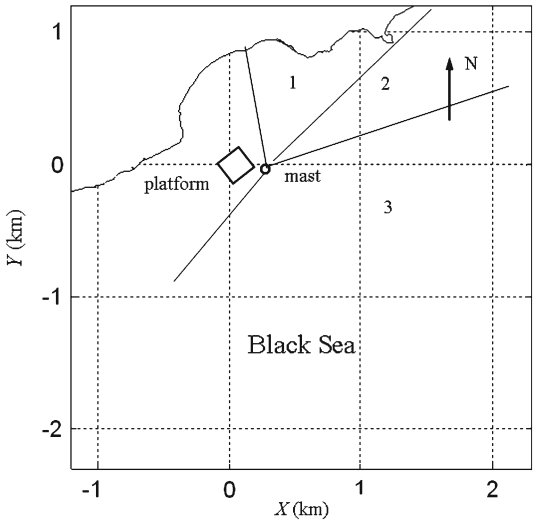

Fig. 1 Map of the experimental area and the wind-direction sectors: sector 1, 2 and 3 indicates respectively offshore, alongshore and onshore direction of wind

estimated according to Britter et al. (1979) (see also, Moat et al. 2006), did not exceed 2–3%, comparable with the accuracy of the wind-speed measurement by the cup anemometers.

The measured wind speed u almost corresponds to the longitudinal component of the wind velocity. If u and v are the longitudinal and the transverse wind velocity components respectively, then to second order in the wind-speed fluctuation:

$$u \approx U + u' + v'^2/2U, \tag{1}$$

where U is the mean longitudinal wind speed, and u' and v' are the fluctuations. For most cases, the standard deviation of the wind speed fluctuations, $\sigma_{u,v}$, normalized by U was small, of order $\sigma_{u,v}/U \propto 10^{-1}$. Thus we may treat the measured wind speed as the longitudinal component of the mean wind velocity and its fluctuation, i.e. $u \approx U + u'$.

The wind profile measurements were accompanied by hourly measurements of the water temperature at 2-m depth, the air temperature and the humidity at 10-m height. In order to estimate the atmospheric stability, the empirical functions suggested by Dyer (1974),

$$\phi_m(\zeta) = 1 + 5z/L \tag{2a}$$

for $L \geq 0$, and

$$\phi_m(\zeta) = (1 - 16z/L)^{-1/4} \tag{2b}$$

for $L \leq 0$ were chosen. The Obukhov length scale L is estimated using a bulk relation, and the heat transfer coefficient $C_{H10} = 1.1 \times 10^{-3}$ for unstable and $C_{H10} = 0.8 \times 10^{-3}$ for stable conditions, and $C_{H10} \approx C_{E10}$ for evaporation were adopted (Large and Pond 1981; Smith 1980; Dupuis et al. 2003). The atmospheric stratification varied from strongly unstable to near-neutral, or in terms of z/L (for $z = 10$ m) $-2.5 < z/L < 0.05$.

The surface displacement was also measured by an array consisting of six wire wave gauges. These data were further utilized for the estimation of frequency-directional wave spectra $F_\eta(f, \theta)$ using the maximum likelihood method (Capon 1969). An example of the observed frequency-directional wave spectrum is presented in Fig. 2. The spectral peak in the wind direction can be treated as wind waves, while swell propagates from the open sea at an angle of 80° relative to the wind direction. The angular spreading of swell energy

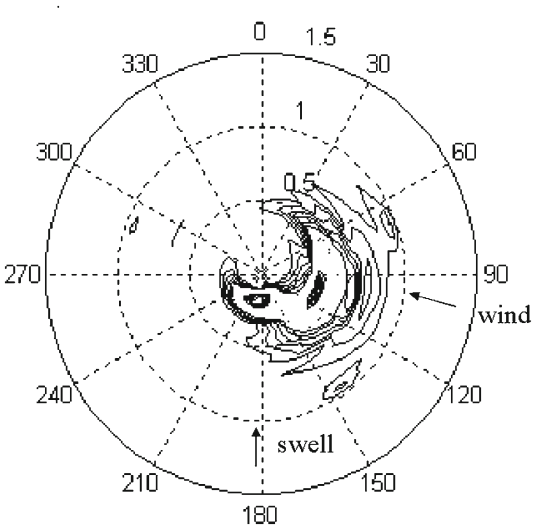

Fig. 2 An example of the directional-frequency wave spectrum at a wind speed $U_{10} = 5.5$ m s^{-1}. *Arrows* indicate the spectral peak of swell and wind waves (spectral direction is indicated as "off")

in Fig. 2 is apparently narrower than for wind waves. In the present study we define the frequency-directional spectrum as:

$$F_\eta(f, \theta) = S_\eta(f)\phi(\theta), \tag{3}$$

where S_η is the frequency spectrum and $\phi(\theta)$ is the angular spectrum. The latter is parameterized as (e.g. Babanin and Soloviev 1987)

$$\phi(\theta) = A\cos^n(\theta - \theta_0), \tag{4}$$

where $|\theta - \theta_0| \leq \pi/2$, A is the normalization coefficient defined by the condition $\int \phi(\theta)d\theta = 1$, and θ_0 is the mean direction of wave propagation. The magnitude of $1/A$ is approximately equal to the half angular spectral width (in radians). For the measurements, parameter n in Eq. 4 varied in the range from 10 to 20, equivalent to an angular width of 45°–30°. More information on the characteristics of the equipment, the data recording and processing can be found in Soloviev et al. (2004) and Soloviev and Ivanov (2007).

3 Experimental Data

In the present study we use data collected for onshore winds, when the MABL properties are typical of open sea conditions. Since swell travels from the open sea, the angle $\beta_0 = \theta_0 - \phi_w$ between the mean directions of the swell θ_0 and the wind ϕ_w is restricted to the range 0° to 150°. Hereafter the directions of wind and swell are defined as the direction of the wind velocity and wavenumber vectors.

3.1 Time Series

Two fragments of time series, where the wind-speed undulation is well correlated with the surface displacement, are shown in Fig. 3 for the following-wind swell, and in Fig. 4 for the opposite-wind swell. In both cases the swell-induced undulations of the airflow are well pronounced, although the phase of the undulations is quite different: for the following-wind swell

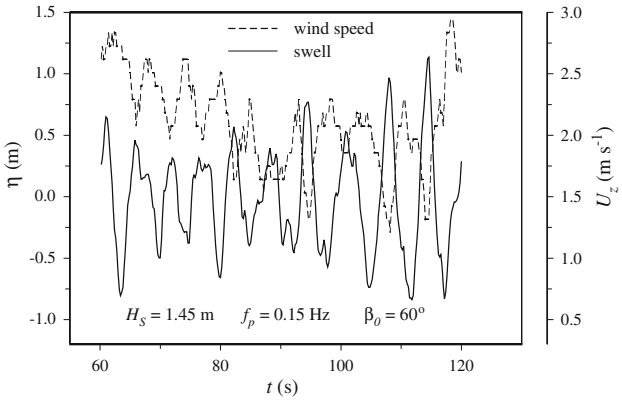

Fig. 3 Fragment of the time series of the sea–surface displacement (*solid line*) and the wind speed (*dashed line*) at $z = 2.95$ m for the following-wind swell. Values for the significant wave height H_S, the peak frequency f_p and the relative angle β_0 between the wind and swell direction are indicated

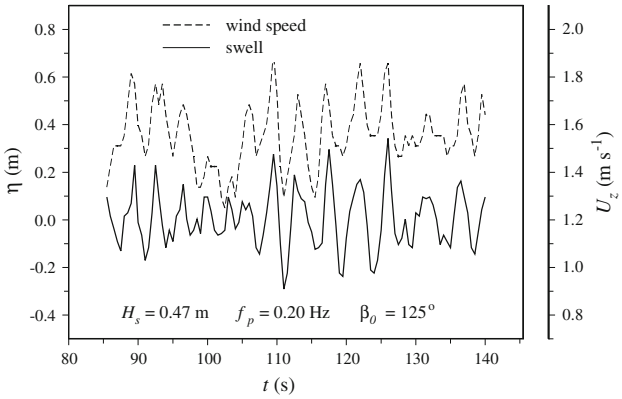

Fig. 4 The same as in Fig. 3, but for $z = 1.35$ m and the opposite-wind swell

the air flow accelerates over troughs, while for the opposite-wind swell the air accelerates over crests.

3.2 Spectral Quantities

Quantitative estimates of the relation between the swell-induced undulation of wind speed and the surface displacement can be made from the standard cross-spectral analysis of time series (see e.g. Jenkins and Watts 1972).

Figure 5 shows spectra of wind velocity fluctuations for various wind and swell conditions. A remarkable, but well-known, feature of these spectra is the existence of the inertial subrange of atmospheric turbulence, associated with the '−5/3' slope. Since the swell-induced undulation in the airflow may disturb the shape of the spectra in the inertial subrange, such an effect is manifest as a local spectral peak at the swell frequency, which is well revealed at the lower levels of measurements, both for the following-wind and the opposite-wind swell cases. Disturbances of the wind spectra by swell are also revealed at the upper levels, although they are much weaker. Wind-speed spectra shown in Fig. 5 can be considered as typical.

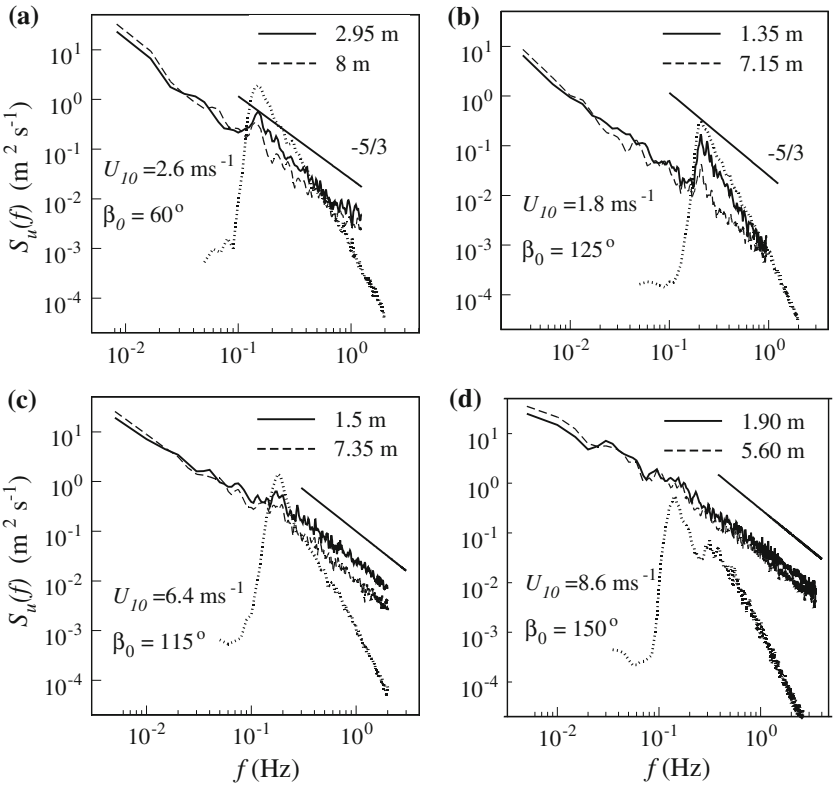

Fig. 5 Frequency spectra of the wind-speed fluctuations at two levels (*solid* and *dashed lines*) and the sea–surface displacement (*dotted lines*, the dimension of wave spectra is m^2 s): **a** the following-wind swell, the same case as shown in Fig. 3; **b** the opposite-wind swell, the same case as shown in Fig. 4; **c**, **d** opposite-wind swell for moderate wind. Height of the anemometers, the wind speed U_{10} at 10-m height, and the angle β_0 between wind and swell are indicated in each panel

Local spectral peaks at the swell frequency are always observed at wind speeds $U_{10} < 6$–7 m s^{-1} except for cases when swell travelled almost cross-wind ($80° < \beta_0 < 100°$). In the wind-speed range 8–10 m s^{-1} the spectral peak at the swell frequency is not expressed due to the high level of turbulence (see Fig. 5d). However, the swell-induced undulation is revealed in the coherence and phase spectra. According to our observations, swell with a significant wave height $H_S \approx 1$–1.5 m and $f_p > 0.12$ Hz induces wind-speed fluctuations near the surface with an amplitude $\tilde{\sigma}_u / U \propto 0.1$, which is comparable to the turbulent fluctuations.

Spectra of the squared coherence $\gamma^2(f)$ and the phase $\Phi(f)$ are defined as

$$\gamma^2 = \left|S_{u\eta}\right|^2 / (S_u S_\eta), \tag{5a}$$

$$\Phi = \arctan\left(S^q_{u\eta} / S^c_{u\eta}\right), \tag{5b}$$

where $S_{u\eta} = S^c_{u\eta} + i S^q_{u\eta}$ is the cross-spectrum of the wind velocity fluctuations and the surface displacement, and $S^c_{u\eta}$ and $S^q_{u\eta}$ are its real and quadrature parts. Vertical profiles of the squared coherence $\gamma^2(f_p)$ for the swell spectral peak frequency are shown in Fig. 6. These data were obtained for different runs for similar β_0 (β_0 varied in the range $\pm 5°$) and wind

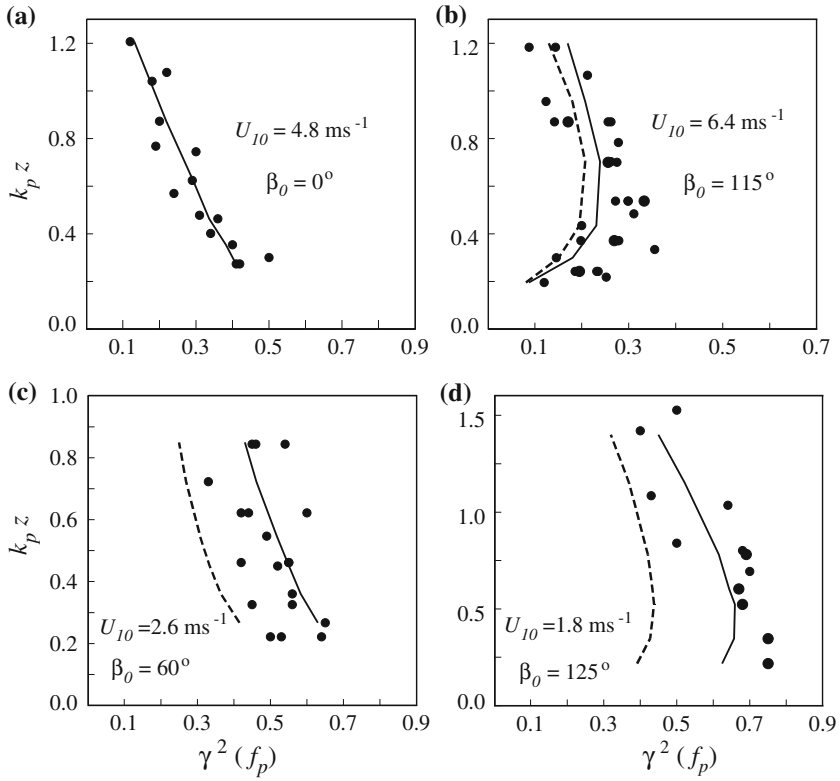

Fig. 6 Vertical profiles of the squared coherence between the wind-speed fluctuations and the surface displacement at the spectral peak frequency f_p. Measurements are shown by *black circles*. *Solid line* are the model calculations according Eq. 18 for the directional spectrum $\propto \cos^{20}\theta$ and *dashed line* for $\propto \cos^2\theta$. The mean wind speed and the angle between the swell and wind directions are indicated in each panel

speed (which varied in the range ± 0.3 m s^{-1}). The coherence decreases with height, except for the case with near cross-wind swell (Fig. 6b). The decrease of the coherence presumably results from the vertical attenuation of the swell-induced undulation. If swell travels close to the cross-wind, the profile of coherence has a pronounced maximum (Fig. 6b), showing that in such conditions the amplitude of the swell-induced undulation should also have a local maximum (see Sects. 3.3 and 4.2 below for a more detailed analysis).

3.3 Amplitude of the Swell-Induced Undulation

Wind-speed fluctuations u' can be presented as the sum of the swell-induced undulation $\tilde{u}$ and random turbulent fluctuations u^t : $u' = \tilde{u} + u^t$. In this case, the spectrum of the total wind-speed fluctuations S_u is the sum of two spectra: $S_u = \tilde{S}_u + S_u^t$. The spectrum of the swell-induced undulations can be found from the cross-spectral parameters as (e.g. Jenkins and Watts 1972)

$$\begin{aligned} \tilde{S}_u(f) &= \left|S_{u\eta}(f)\right|^2 / S_\eta(f) \\ &= \gamma^2(f) S_u(f). \end{aligned} \tag{6}$$

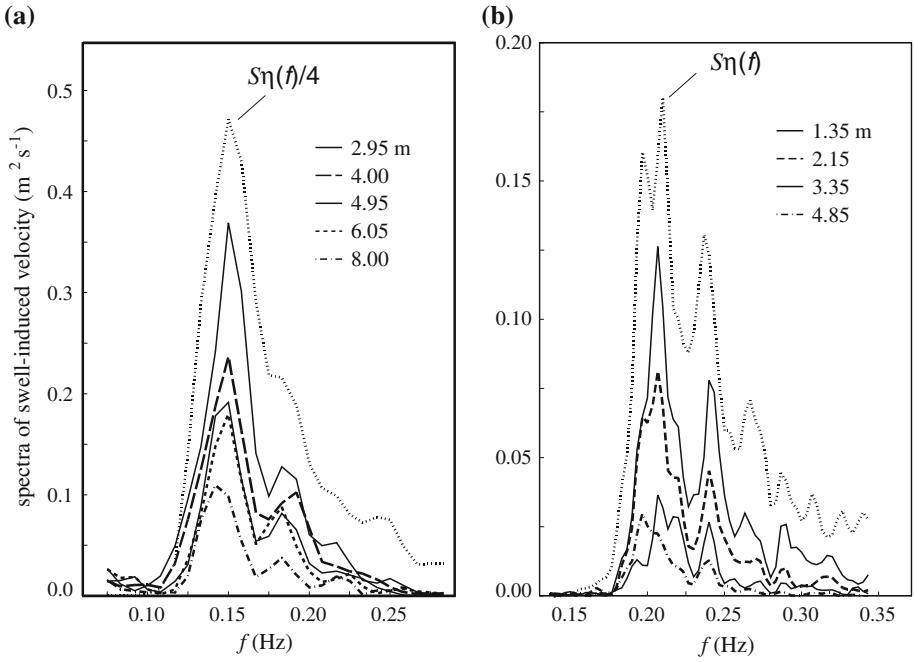

Fig. 7 Spectra of the swell-induced wind speed undulation calculated according to Eq. 6: **a** for the following-wind swell (the same data as in Fig. 3); **b** for the opposite-wind swell (the same data as in Fig. 4). Lines of different style correspond to measurements at different heights (indicated in the right-upper corner of panels). The surface displacement spectra $S_\eta(f)$ are shown by *dotted line* (in order to fit the velocity spectrum, $S_\eta(f)$ in (**a**) is reduced by a factor of 1/4)

Examples of spectra based on Eq. 6 for the following-wind and the opposite-wind swell are shown in Fig. 7. On the whole, the shape of the spectra $\tilde{S}_u$ is similar to the swell spectrum, but the spectral level decreases with height. With careful inspection one also sees a shift in the spectral peak frequency of $\tilde{S}_u$ towards lower frequency with increasing altitude, i.e. the high frequency undulations are filtered out at higher altitudes.

In order to suppress the large sampling variability of the coherence and to take into account the "finite" width of the velocity spectra (see Fig. 7), we assigned the standard deviation as a measure of the amplitude of the swell-induced undulations:

$$\tilde{\sigma}_u = \left[\int_{\Delta f} \tilde{S}_u(f) df \right]^{1/2} , \tag{7}$$

where $\tilde{S}_u(f)$ is given by Eq. 6 and Δf is the spectral interval overlapping the peak frequency f_p. To determine Δf, we note the following: the main errors in the estimates of $\tilde{S}_u$ in Eq. 6 come from the variance of estimates of γ^2 (Eq. 5a) and its bias $\Delta\gamma^2$. The former can effectively be reduced by averaging (see Eq. 8 below), while the reduction of the bias needs special attention. For the cosine window the bias $\Delta\gamma^2$ is defined as (Jenkins and Watts 1972)

$$\Delta\gamma^2(f) \approx 0.75\tau/T + 0.126\gamma_0^2\tau^{-2}\,(\partial\Phi/\partial f)^2 , \tag{8}$$

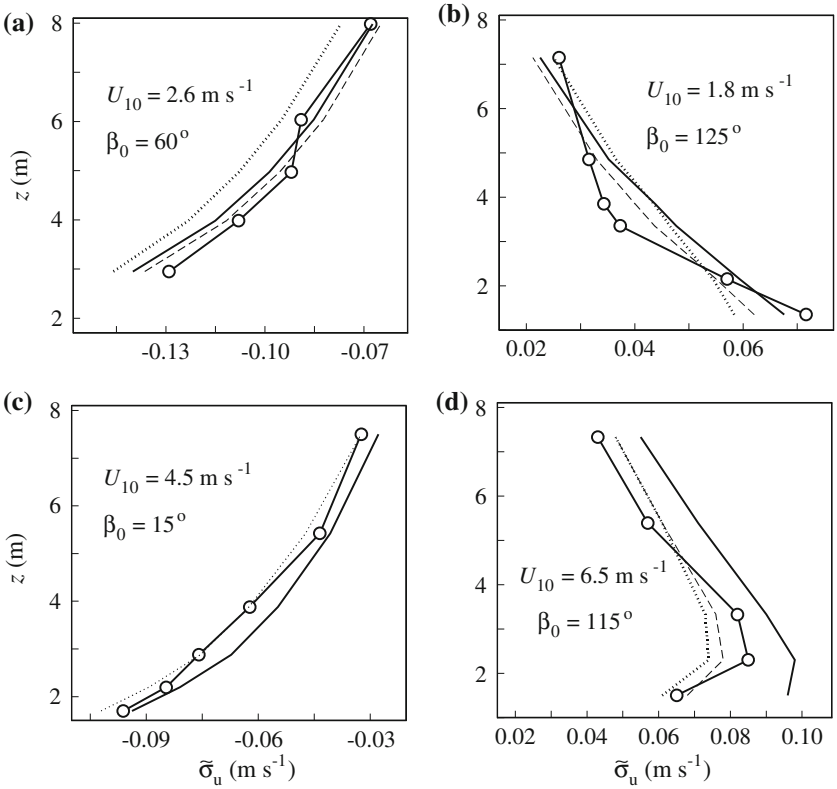

Fig. 8 The vertical profiles of the amplitude (the standard deviation $\tilde{\sigma}_u$) of the wind-speed undulation. Curves with *open circles* are the experimental estimate defined by (7) with (6). *Solid line* is the model $\tilde{\sigma}_u$ calculated according to Eq. 7 with (13) and according to Eq. 7 with (14) (*dashed line*) for the measured wave spectra $S_\eta(f)$ with the angular spreading $\cos^{20}\theta$. *Dotted line* shows the model calculations for the 'monochromatic' swell, Eq. 17. Notice that negative/positive values of $\tilde{\sigma}_u$ imply that the wind-speed undulation is in antiphase/phase with the surface displacement. The wind speed at the reference level and the swell direction (in respect to the wind direction) are indicated

where τ is the maximum lag of the correlation function, T is the length of the time series, and $\gamma_0^2(f)$ is the "true" coherence. The first term in Eq. 8 is the bias due to the averaging and for typical $\tau = 10^2$ s and $T = 2 \times 10^3$ s it is about $\Delta\gamma^2 \approx 0.03$, i.e. negligible. In contrast, the second term in Eq. 8 may lead to large false peaks if the behaviour of the phase shift (Eq. 5b) over f is "unstable". Therefore, to reduce the errors in estimates of $\tilde{S}_u$ defined by Eq. 6, we considered only that frequency range Δf where the condition $\Phi(f) \approx$ constant was fulfilled. This approach is valid for the analysis of data containing one dominating wave system. Therefore, below we analyze only data collected at the wind speed $U_{10} < 6$–7 m s^{-1}, and when one system of swell with $H_S \geq 0.3$ m was observed. Further to these data, we also consider eight additional cases collected at higher wind speeds 8–10 m s^{-1}, when wind waves and the opposite-wind swell are well separated, as in Fig. 5d. In total, 55 runs for the following-wind and 35 runs for the opposite-wind swell have been analyzed.

Examples of the vertical profiles of the amplitude of the wind-speed undulations, $\tilde{\sigma}_u$, calculated using (7) with (6) are shown in Fig. 8. Data shown in Fig. 8a correspond to the case presented before in Figs. 3 and 5a, and data in Fig. 8b correspond to the case presented in

Figs. 4 and 5b. Other profiles in Fig. 8 illustrate behaviour of the wind-speed undulations for the following-wind swell at higher wind speed (Fig. 8c) and for swell travelling in the direction near to the cross-wind (Fig. 8d) presented in Fig. 5c. Notice that for the following-wind swell (Fig. 8a, c) observed phase shifts between the wind-speed undulations at different altitudes and the surface displacements were about 180°, while for the opposite-wind swell (Fig. 8b, d) they are about 0°. In Fig. 8 these phase shifts are adopted as the sign of the amplitude—they are negative for the following-wind swell and positive for the opposite-wind swell. In the case of the following-wind swell (Fig. 8a, c) the swell-induced undulations always attenuate monotonically with height. However the behaviour of the $\tilde{\sigma}_u$ profile for the opposite-wind swell (Fig. 8b, d) may be quite different and depend on the angle between swell and wind directions, the swell height and atmospheric stability. It was found that the local maximum in profiles of the wind-speed undulations has always appeared if the opposite-wind swell travels close to the cross-wind direction (e.g. $\beta_0 < 120°$) as shown in Fig. 8d. A similar maximum can be observed at any angle for the opposite-wind swell if its amplitude is large enough. As discussed below, this effect is typical of measurements of wind-speed undulations at fixed levels induced by the opposite-wind swell under near-neutral conditions.

4 Analysis of Data

4.1 Model Approach

Before proceeding with analysis, we introduce a "model tool" that will facilitate the analysis of experimental data on a systematical basis. According to the rapid distortion theory (Belcher and Hunt 1993), the turbulent airflow over the wave can be separated into two regions—the inner (at $z < l$) and the outer (at $z > l$) regions. At an arbitrary direction between the wind and the wave, the scale l is estimated as $kl = (1 + \cos^2\beta)u_*/|U\cos\beta - c|$, where u_* is the air friction velocity and c is the phase velocity. The order of l varies as: $kl \propto 10^{-2}$ for swell, $kl \propto 1$ for wind waves with $c \approx U$, and $kl \propto 10^{-1}$ for slow wind waves, $c \ll U$ (Kudryavtsev and Makin 2004; see their Fig. 1). The inner region has an important physical meaning: it distinguishes the region in the boundary layer above the wave where disturbances of the turbulent stress (and other characteristics of turbulence), caused by the interaction of the air flow with the surface, are confined. Consequently, in the outer region the wave-induced variation of turbulent characteristics vanishes, and the dynamics of the outer region can be considered as the dynamics of an inviscid airflow. Our data were collected well above swell crests, at heights satisfying the condition $kz > 0.1$, i.e. these measurements can be treated as made in the outer region of the MABL.

The classical problem on the dynamics of an inviscid shear flow over a wavy surface with displacement $\eta = a\exp[i(kx - \omega t)]$ (a is the amplitude) is based on the solution of the Rayleigh equation. In the context of wind-wave generation, this equation had been first studied by Miles (1957). Kudryavtsev et al. (2001) suggested the simplified model of the turbulent atmospheric boundary layer above waves, where they showed that in wave-following coordinates $x_3 = z - \eta(x,t)\exp(-kz)$ the wave-induced variation of the horizontal velocity inside the outer region can be described as

$$\hat{u}_1/ka = (U\cos\beta - c)e^{-kx_3} + 2\cos\beta\int_{x_3}^{\infty} U_z' e^{-kx_3}dx_3, \tag{9}$$

where $\hat{u}_1$ is the amplitude of the wind-velocity component in the direction of the swell wave-number vector, β is the angle between the wind and swell directions, and $U'_z = \partial U/\partial z$. Correspondingly, the variation of the wind-velocity component parallel to the wave crest vanishes, i.e. $\hat{u}_2/ka = 0$. In Eq. 9 the second term describes the impact of the vorticity of the mean flow; this term is important for "slow" waves, when $c/U \ll 1$, but for swell its effect on $\hat{u}_1$ should be small.

To the first order on ak, Eq. 9 has the same form in the Cartesian coordinate system (one needs simply replace x_3 by z) and can be used to simulate the wind-speed variations measured in our experiments. On the other hand, measurements were made at fixed heights, and therefore we have to take into account the wind-speed variation caused by the displacement of the mean flow streamlines: $\tilde{u}_\eta = -\eta U'_z \exp(-kz)$ (Kitaigorodskii 1970; Kudryavtsev and Makin 2004). Then, keeping in mind that the variation of the wind velocity in the swell direction, $\tilde{u}_1$ (defined by Eq. 9), and the longitudinal component, $\tilde{u}$, are linked as $\tilde{u} = \tilde{u}_1 \cos\beta$, we obtain the following relation for the amplitude of the wind-speed undulation $\hat{u}$ in the fixed coordinate system (measured in our experiments):

$$\hat{u}/ak = \hat{U}_u + \hat{U}_\eta, \tag{10a}$$

$$\hat{U}_u = (U\cos\beta - c)\cos\beta \cdot e^{-kz} + 2\cos^2\beta \int_z^\infty U'_z e^{-kz} dz, \tag{10b}$$

$$\hat{U}_\eta = -k^{-1} U'_z e^{-kz}, \tag{10c}$$

where $\hat{U}_u$ is the wind-speed amplitude at a given height scaled by the wave steepness ak, $\hat{U}_\eta$ is the amplitude of the "artificial" component caused by the vertical wave-induced displacement of shear flow in respect to the fixed sensor. The total undulation $\tilde{u}$ is defined as $\tilde{u} = ak(\hat{U}_u + \hat{U}_\eta)\exp[i(kx - \omega t)]$, where only the real part has a physical meaning. According to (10), for the following (opposite)-wind swell the amplitude of the wind-speed undulation is negative (positive), i.e. they are in antiphase (in phase) with the surface displacement as observed and shown in Figs. 3 and 4.

4.2 Model for Measured Spectral Quantities

Equations 10 can be used to build the spectral characteristics measured in the experiment. For the wave spectrum defined by (3), the cross-spectrum $S_{u\eta}$ of the wind-speed undulations and the surface displacement reads

$$S_{u\eta}(f) = \hat{U}_M k S_\eta(f), \tag{11}$$

where $\hat{U}_M$ is the transfer function integrated over the azimuth:

$$\hat{U}_M = \int (\hat{U}_u + \hat{U}_\eta)\phi(\beta - \beta_0) d\beta, \tag{12}$$

where we take into account that $\beta - \beta_0 = \theta - \theta_0$. Then using (11), the model spectrum of the wind-speed undulations simulating the measured estimate $\tilde{S}_u(f)$ defined by (6) reads

$$\begin{aligned} \tilde{S}_u^M(f) &= \left|S_{u\eta}(f)\right|^2 / S_\eta(f) \\ &= \hat{U}_M^2 k^2 S_\eta. \end{aligned} \tag{13}$$

We treat this spectrum as the "measurable" one, which can be estimated from measurements of the surface elevation and the wind-speed profile. The phase shift between the swell-induced wind undulations and the surface elevation is defined by the sign of $\hat{U}_M$: if it is

positive/negative, the phase shift is 0°/180°. Referring to (12) with (10) one can see that the wind-speed undulations are in phase with the surface displacement for the following-wind swell, and vice-versa for the opposite-wind swell, as was observed. Note that the spectrum (13) differs from the "real" frequency spectrum of the 2D wind-speed undulations defined as $\tilde{S}_u^R(f) = \int \hat{u}^2(f,\beta)d\beta$. With the use of (10) this spectrum is

$$\tilde{S}_u^R(f) = U_R^2 k^2 S_\eta(f), \tag{14}$$

where U_R is the other spectral transfer function:

$$\hat{U}_R^2 = \int \left(\hat{U}_u + \hat{U}_\eta\right)^2 \phi(\beta - \beta_0)d\beta. \tag{15}$$

Comparing (14) and (13) we see that the "measurable" spectrum (13) coincides with the "real" one (14) if the angular spreading of swell is narrow; in general they are different. If one assumes that the swell spectrum is very narrow both in frequency and angular domain, i.e.

$$F_\eta(f,\theta) = \sigma_\eta^2 \delta\left(f - f_p\right)\delta\left(\theta - \theta_0\right), \tag{16}$$

then the standard deviation of the wind-speed undulations (7) is reduced to

$$\tilde{\sigma}_u / \left(k_p \sigma_\eta\right) = \left|\hat{U}_u^p + \hat{U}_\eta^p\right|^2. \tag{17}$$

where $\hat{U}_u$ and $\hat{U}_\eta$ are defined by (10), and the superscript "p" means that they are specified for the spectral peak parameters k_p, c_p and β_0.

In order to simulate the coherence defined by (5a), we note that the spectrum of total wind-speed fluctuations S_u is the sum of the swell-induced undulation spectrum $\tilde{S}_u^R$ and the spectrum S_u^t of turbulent fluctuations. Then, with the use of (11) and (14), the model for the coherence is

$$\gamma^2 = \frac{\hat{U}_M^2}{\hat{U}_R^2 + k^{-2} S_u^t / S_\eta}, \tag{18}$$

where S_u^t is defined in Sect. 4.3.2.

To simulate measurements the model "input parameters" were specified in accordance with observations, namely: the mean wind-speed profile and the swell spectrum are specified as measured; the wind-speed shear in (10) is defined through Monin-Obukhov similarity theory for the shear flow $\kappa z U_z' / u_* = \phi_m(z/L)$, where $\kappa = 0.40$ is the von Karman constant, $\phi_m(z/L)$ is the empirical function (2) proposed by Dyer (1974).

4.3 Results

4.3.1 Variations of the Wind Direction

Variations of the airflow direction with periods exceeding $t_h = h/u_*$ ($h = 8$ m is the height of the upper anemometer) influence the measured wind-speed undulations. At $u_* = 0.1$–0.3 m s^{-1} the time scale t_h is in the range: $t_h = 30$–80 s. Apparently, the impact of the airflow direction variability on the wind-speed undulations is equivalent to the impact of the swell direction. According to measurements, the standard deviation σ_ϕ^w of the wind direction at 21-m height at $U_{10} > 5$ m s^{-1} was in the range $\sigma_\phi^w = 0.07$–0.12 rad ($4 - 7°$), and $\sigma_\phi^w =$ 0.09–0.2 rad ($5 - 12°$) at lower wind speeds. A major part (about 80–90%) of σ_ϕ^w was provided by fluctuations with periods $T > 10$ s. We took this effect into account through the

parameterization of the swell angular spectrum (4), describing it as $\phi(\theta) \propto \cos^{20}\theta$. In this case the standard deviation of the swell direction

$$\Delta\beta^2 = \int (\beta - \beta_0)^2 \, \phi \, (\beta - \beta_0) \, d\beta \tag{19}$$

is $\Delta\beta = 0.22$ rad (or $\Delta\beta = 12.5°$) which "absorbs" the wind-direction variability.

4.3.2 Coherence

Since the coherence plays a key role in the splitting of the wind-speed fluctuations for the swell-induced and turbulent components, it is worthy first to compare the model prediction (16) with the experimental estimates shown in Fig. 6. As already mentioned, the remarkable feature of the observed velocity spectra (see Fig. 5) is the existence of the inertial subrange, which is associated with the "−5/3" slope. Therefore, in order to assess γ^2 we assume that the turbulent spectrum S_u^t in (18) can be approximated by the Kolmogorov spectrum for the inertial subrange $S_u^t(k) = c_K \varepsilon^{2/3} k^{-5/3}$ with the constant $c_K \approx 0.53$ (Edson and Fairall 1998). The wavenumber k is defined through Taylor's hypothesis $k = 2\pi f/U$, and the dissipation rate is $\varepsilon \approx u_*^3/z\kappa$, i.e.

$$S_u^t(f, z) = c_u u_*^2 U^{2/3} f^{-5/3} z^{-2/3}, \tag{20}$$

where $c_u = c_K(2\pi\kappa)^{-2/3}$. In order to simulate observations we have utilized in (18) the experimental data for f_p, $U(z)$, u_* and $S_\eta(f_p)$, and performed the model calculation for the "wide" and the "narrow" angular spectrum of swell ($\sim \cos^2\theta$ and $\sim \cos^{20}\theta$ respectively). Model calculations are shown in Fig. 6; calculations with the "narrow" spectrum are much more consistent with data, and so the spectrum $\phi \propto \cos^{20}\theta$ is used further for the model simulation.

4.3.3 Amplitude of the Wind-Speed Undulation

Model simulations of data in terms of the standard deviation of the wind-speed undulation (defined by (7)) for "measurable" (13) and "real" (14) spectra, as well as for "monochromatic" swell (Eq. 17), are shown in Fig. 8 for the following- and opposite-wind swells. As follows from this figure, all variants of the calculation are consistent with measurements on a quantitative level, reproducing correctly the magnitude of the wind-speed undulation at different heights. The exception is the case of the near cross-wind swell (Fig. 8d) where calculations based on the "real" spectrum (14) with (15) exceed both the data and other models by a factor of 1.5.

According to the model (10), the well-pronounced peak in the $\tilde{\sigma}_u$ profile for the opposite-wind swell results from the contribution of the "artificial" wind-speed undulation (the term $\hat{U}_\eta$ in (10c)) caused by the vertical displacement of the shear flow through a fixed wind sensor. For the opposite-wind swell the term $\hat{U}_u$ is positive, therefore the negative term $\hat{U}_\eta$ (which rapidly increases towards the surface) leads to the formation of the local peak in the $\tilde{\sigma}_u$ profile. For the following-wind swell, a similar peak in the $\tilde{\sigma}_u$ profile is not generated because both $\hat{U}_u$ and $\hat{U}_\eta$ are negative. Note that the contribution of the "artificial" term $\hat{U}_\eta$ to the wind undulation depends on atmospheric stability. At low wind speeds and unstable stratification, when wind shear is almost zero, its contribution is small and the local peak does not appear, as seen in Fig. 8b.

Figure 9 shows the experimental estimates of the wind-speed undulation $\tilde{\sigma}_u$ for the whole dataset against the model predictions performed for two spectral models (13) and (14), with

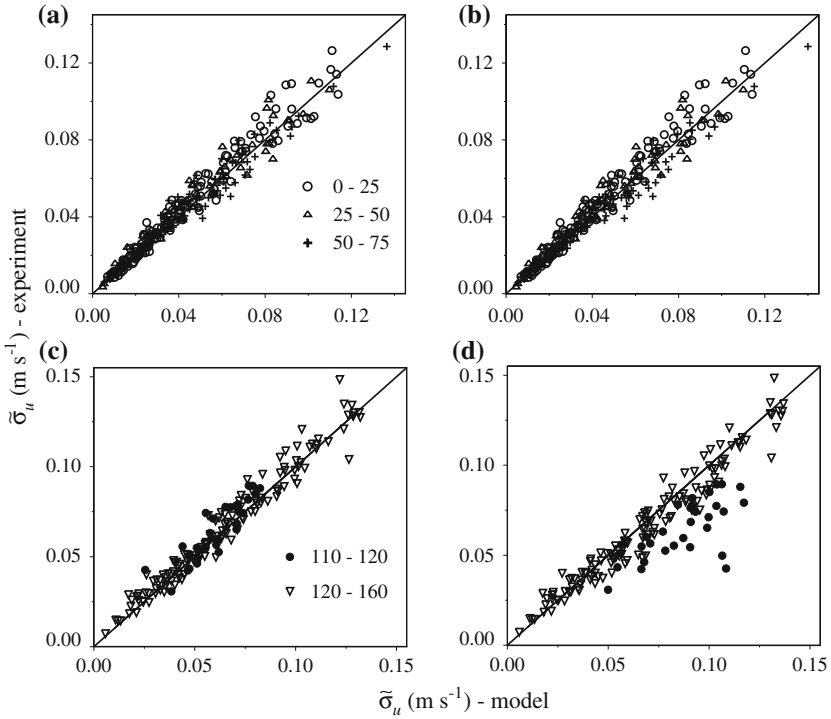

Fig. 9 The model simulation of the standard deviations of the swell-induced wind-speed undulation versus the measured one for the following-wind swell (**a**, **b**), and for the opposite-wind swell (**c**, **d**). The model estimate is calculated for the measured frequency swell spectra with the angular spreading $\propto \cos^{20}\theta$ for the "measurable" model (13) and the "real" model (14), which are shown in (**a**, **c**) and (**b**, **d**) respectively. *Symbols* indicate the range of the angle β_0 (in degrees) between the mean directions of wind and swell. *Solid line* is the one-to-one relation

the "realistic" swell angular spectrum $\propto \cos^{20}\theta$. Calculations shown in Fig. 9a, c for the measurable spectra (13) are well consistent with data for all swell directions. The "monochromatic" swell model (17) is also in agreement with data (not shown). Model simulations based on the "real" spectrum (14) are consistent with data for the following-wind swell, while for the opposite-wind swell the discrepancy is significant, especially for cases when swell travels near the cross-wind direction (Fig. 9d). This discrepancy shows that the measured wind-speed undulation (derived as coherent with the surface elevation) may underestimate the energy of the "real" undulation induced by swell in the airflow. From the model point of view this difference results from the different angular spreading of $\hat{U}_M$ and $\hat{U}_R$ predicted by Eqs. 12 and 15, which in turn implies a different response of the wind-speed undulation to the swell direction. For most angles the measured and real amplitudes are very similar (see Fig. 9). However at the direction close to the cross-wind the measured variance can significantly underestimate the energy of the swell-induced undulation existing in the airflow.

The same dataset is shown in Fig. 10 as a function of the vertical coordinate $k_p z$. The model and measured amplitudes $\tilde{\sigma}_u$ are scaled by the factor $\tilde{\sigma}_{u0} = k_p \sigma_\eta \left|\left(U\cos\beta_0 - c_p\right)\cos\beta_0\right|$, which is the leading term for the wind-speed undulation (10) near the surface ($k_p z \ll 1$) if swell is fast enough, i.e. $U/c_p \ll 1$. As follows from Fig. 10a, c, the data at such scaling effectively collapse near the line $\exp(-k_p z)$. The model simulations scaled by the same factor exhibit a form that is very similar to measurements (compare the right and left panels of

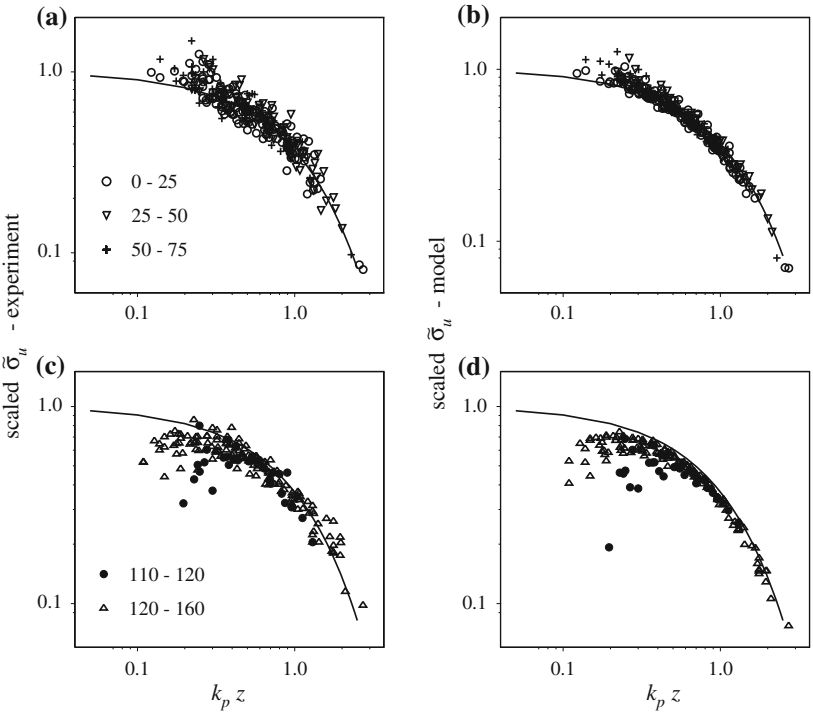

Fig. 10 The vertical profiles of the wind-speed undulation induced by the following-wind (**a**, **b**) and the opposite-wind (**c**, **d**) swell scaled by the factor $\tilde{\sigma}_{u0} = k_p \sigma_\eta \left| (U \cos\beta_0 - c_p) \cos\beta_0 \right|$. (**a**, **c**) show the experimental estimate (7), and (**b**, **d**) the model simulation according (13). *Symbols* are the same as in Fig. 9. *Solid line* is $\exp(-k_p z)$

Fig. 10). The deviation of both the model and data from $\exp(-k_p z)$ is most pronounced at small $k_p z$, and apparently results from the increasing contribution of the "artificial factor" $\hat{U}_\eta$ to the airflow undulation. For the opposite-wind swell this term leads to the local peak in $\tilde{\sigma}_u$, as discussed above.

We refer to $\hat{U}_\eta$ as "artificial" because the impact of the vertical displacement of the shear flow through a fixed sensor on $\tilde{\sigma}_u$ is only important in the context of a proper interpretation of measurements. From the point of view of the study of the airflow dynamics, it is more important to look at the swell-induced undulation in the wave-following coordinate system. In order to transform measurements into such a coordinate system, we have subtracted the term $kS_\eta \hat{U}_\eta$ (where $\hat{U}_\eta$ is defined by (10c)) from the experimental estimates of the cross-spectrum $S_{u\eta}$. This residual spectrum

$$\tilde{S}_u(f) = \left| S_{u\eta} - kS_\eta \hat{U}_\eta \right|^2 / S_\eta(f) \tag{21}$$

can further be treated as the spectrum of the wind-speed undulation in the wave-following coordinate system. The experimental estimates of the standard deviation $\tilde{\sigma}_u$ defined by (7) with (21) and scaled as before by the factor $\tilde{\sigma}_{u0}$ are shown in Fig. 11. The standard deviation of wind-speed undulations induced by the monochromatic swell (16) in the wave-following coordinate system is

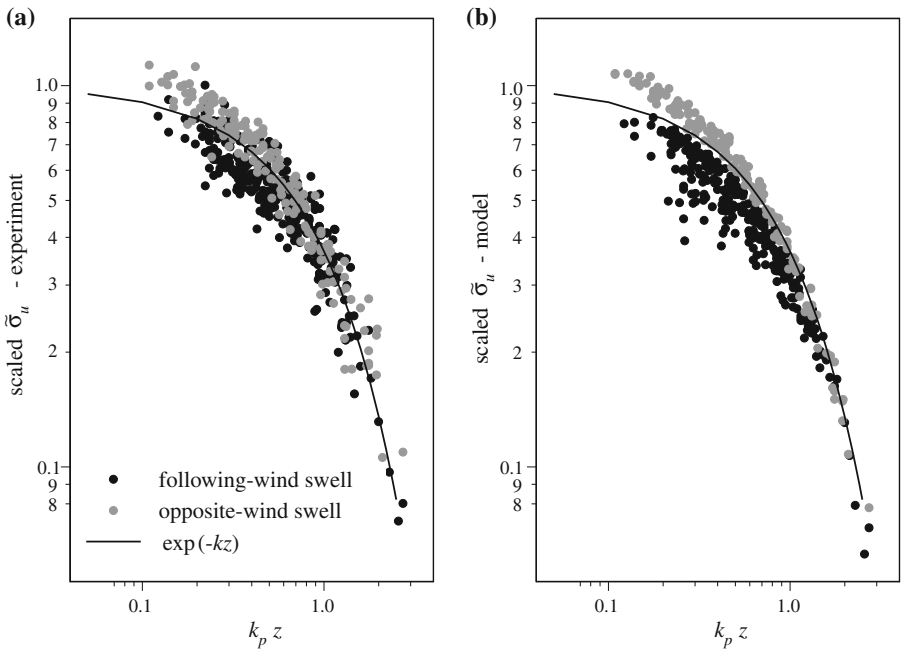

Fig. 11 The vertical profiles of the standard deviation $\tilde{\sigma}_u$ of the swell-induced undulation in the wave-following coordinate system scaled by the factor $\tilde{\sigma}_{u0} = k_p \sigma_\eta \left|\left(U\cos\beta_0 - c_p\right)\cos\beta_0\right|$: **a** the experimental estimate, **b** the model simulation according (13). Converting of the wind-undulation spectra from the fixed to the wave-following coordinate system was done using (21). *Solid line* is $\exp(-k_p z)$ that corresponds to the profile of the wind-speed undulation obeying the potential streamline law described by the first term in Eq. 22. *Black circle* indicates data for the following-wind swell, and *grey circle* for the opposite-wind swell

$$\tilde{\sigma}_u / \left(k_p \sigma_\eta\right) \approx \left| \left(U\cos\beta_0 - c_p\right)\cos\beta_0 \cdot e^{-k_p z} + 2\cos^2\beta_0 \int_z^\infty U_z' e^{-k_p z} dz \right|. \qquad (22)$$

If the swell is fast (the parameter U/c_p is small) the wind-speed undulations should be approximately described by the first term in Eq. 22. Referring to Fig. 11 we see that measured estimates of $\tilde{\sigma}_u$ in the wave-following coordinate system are scattered around the curve $\exp(-k_p z)$, i.e. the observed undulations obey the "potential streamline law" predicted by the first term in Eq. 22. On the other hand, the remarkable feature of these data is that the undulations induced by the opposite- and following-wind swells are located on different sides of the exponent. We may assume that this feature can be interpreted as the influence of the vorticity of the dominant flow on the wave-induced undulation predicted by the second term in Eq. 22. As anticipated, this effect is not significant, but nevertheless the model (22) reproduces the observed peculiarities at the quantitative level.

5 Discussion

The analysis of data presented above showed that the observed undulation of wind speed obeys the quasi-laminar theory for the wave-induced undulation in a shear flow. In this context one can conclude that the vertical domain of measurements (ranged from $k_p z = 0.1$

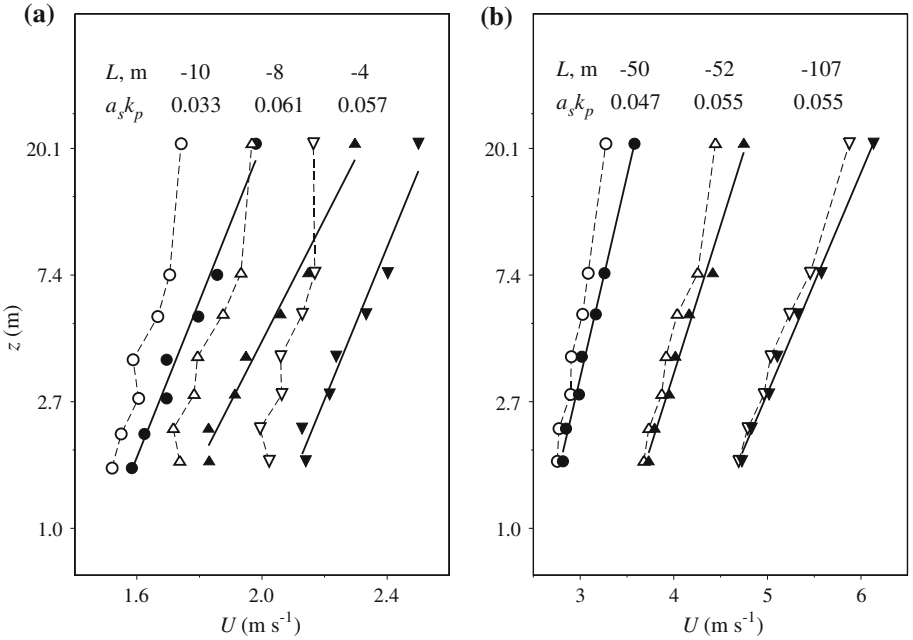

Fig. 12 The wind-speed profiles in log-linear coordinates for very low (**a**) and low (**b**) wind speed above the following-wind swell ($H_S = 0.6$–0.7 m and $f_p = 0.17$–0.20 Hz) propagating at the angle of $0 - 20°$ relative to the wind direction. *Dashed line* with *open symbols* is the measured profiles; *solid line* with *filled symbols* is the "equivalent" wind profiles for neutral conditions. The Obukhov scale L and the swell steepness $a_s k_p$ (where $a_S = H_S/2$) are indicated in the figure for each profile

to $k_p z = 3$) belongs to the outer region of the turbulent boundary layer where the swell-induced momentum flux vanishes. Though the dynamics of the outer region are affected by swell (via the change in magnitude of the turbulent momentum flux due to the momentum pumping from swell to the MABL), its mean properties correspond to Monin-Obukhov similarity theory. Nevertheless, the effect of distortions on the similarity theory by swell has been revealed in a number of earlier field experiments (e.g. Drennan et al. 1999; Smedman et al. 1999; Miller 1999; Rutgersson et al. 2001) and in model simulations by Sullivan et al. (2008). In this section we present the mean properties of the boundary layer observed in our experiment.

The wind-speed profiles in the layer 1.7–20.8 m for the following-wind swell are shown in Fig. 12. The measured profile $U(z_i)$ was transformed to the "equivalent" wind profile $U_N(z_i) = U(z_i) + \frac{u_*}{\kappa}\Psi\,(z_i/L)$ for the neutrally stratified boundary layer, where $\Psi(z_i/L)$ is a stability function (e.g. Paulson 1970). The original profile was fitted to the log-linear function $U(z_i) = a + b \ln z_i$ and using empirical functions (2) (supplemented with the standard bulk relations), the consistent values for friction velocity $u_* = b\kappa$, the Obukhov length scale L, the surface roughness scale $z_0 = \exp(-a/b)$ and the wind-speed profile $U_N(z_i)$ were calculated iteratively. As follows from Fig. 12, there is no longer a systematic deviation of $U_N(z_i)$ from the log profile, which could be associated with the impact of swell on the wind profile. A small scattering of $U_N(z_i)$ is within the measurement error, and the accuracy of u_* derived from the wind profile is within 15%.

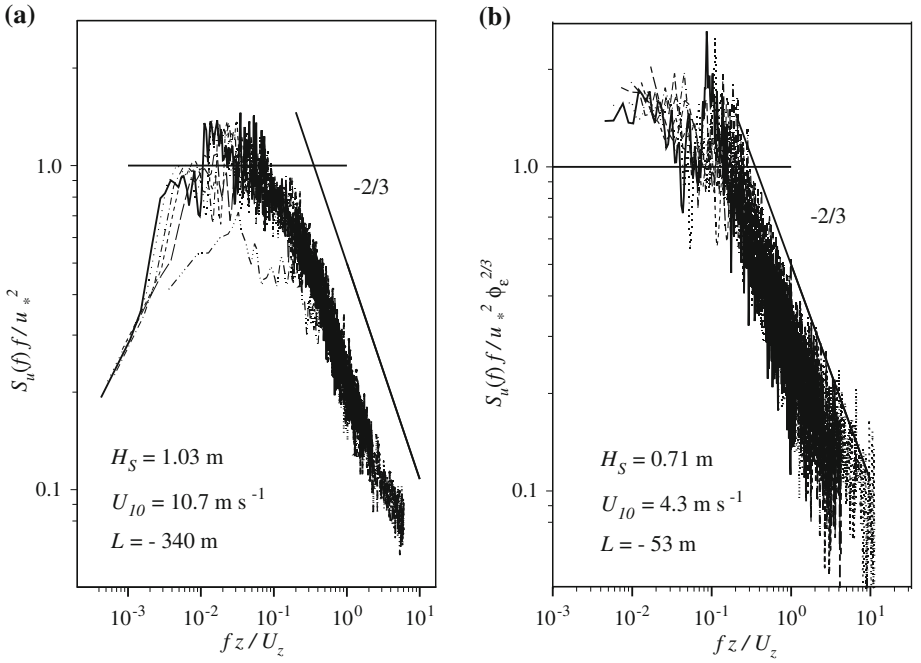

Fig. 13 Normalized spectra of the horizontal velocity at seven heights in the range 1.7–20.8 m versus the dimensionless frequency: **a** the opposite-wind swell ($\beta_0 = 140°$) at high wind speed; **b** the following-wind swell ($\beta_0 = 0°$) at low wind speed condition. Spectra are normalized by u_* (derived from the wind profile) and by the dimensionless dissipation rate ϕ_ε. The length of time series is 120 min (**a**) and 60 min (**b**)

An important feature of the equilibrium turbulent boundary layer is the existence of the universal spectra of turbulence (e.g. Kaimal et al. 1972). The normalized spectra of the horizontal wind velocity fluctuations at seven levels shown in Fig. 13 correspond to the following cases: panel (a) swell with $H_S = 0.69$ m and $f_p = 0.14$ Hz travels at the angle of 140° relative to the direction of "strong" wind, the significant wave height and the spectral peak frequency of wind waves are $H_S = 0.72$ m and $f_m = 0.27$ Hz, the atmospheric stability is approximately neutral; panel (b) swell with $H_S = 0.71$ m and $f_p = 0.20$ Hz travels along the wind direction at low wind speed, the atmospheric stratification is slightly unstable. Spectra are normalized by u_* (derived from the wind profile measurements) and by the dimensionless dissipation rate function: $\varepsilon\kappa z/u_*^3 = \phi_\varepsilon = \phi_m - z/L$. In both cases the normalized spectra are almost collapsed in the inertial subrange $f \geq 0.2U_z/z$ and follow the slope '−2/3'. The level of spectra in the inertial subrange is independent of height and swell. In the intermediate range $fz/U_z \approx 10^{-2}$–10^{-1}, which supports most of the turbulent stress, the spectra also have approximately the same level.

The merging of spectra in the inertial subrange means that the dissipation rate is $\varepsilon \propto z^{-1}$ and the inertial-dissipation (ID) method can also be adopted for the turbulent stress estimation. Comparison of the friction velocity estimates (average over heights) obtained by the wind profile and the ID methods are shown in Fig. 14. On average, values of the friction velocity estimated by the profile method are about 10% larger than those estimated by the ID method, implying that production of the turbulent kinetic energy exceeds dissipation at moderate and strong winds (see also Garratt 1972; Edson and Fairall 1998). However, at low wind speeds (<6 m s^{-1}) for which most of results were obtained, the difference between

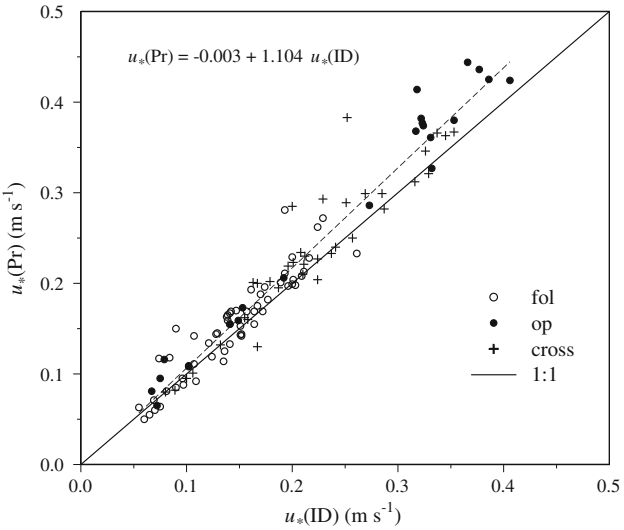

Fig. 14 Comparison of the friction velocity estimates obtained by the wind-profile and the inertial dissipation (ID) method for different swell conditions. The ID estimate of u_* is averaged over all heights. Different *symbols* indicate the direction of swell in respect to the wind direction. *Solid line* is one-to-one relation. *Dash line* is the linear regression of data

the profile and the ID methods is almost negligible. This fact implies that at low wind conditions in the presence of swell the observed part of the MABL (from $k_pz = 0.1$ to $k_pz = 3$) belongs to the equilibrium boundary layer governed by a balance of the local production and dissipation. According to measurements the part of the MABL that is directly affected by swell (i.e. the layer where the swell-induced momentum and energy fluxes are confined) is located presumably below the level $k_pz = 0.1$.

The drag coefficient $C_{D10} = (u_*/U_{10N})^2$ estimated by both methods is shown in Fig. 15 as a function of the neutral wind speed. The empirical relationships proposed by Smith (1980) and Yelland and Taylor (1996) for open ocean conditions are also shown for the comparison. At moderate wind speeds our estimates exceed systematically the empirical relations. A plausible reason is that our data were collected for undeveloped wind waves; the inverse wave age of wind waves for all the data points was about 2. As anticipated, the scatter of the drag coefficient increases with a decrease in the wind speed. Detailed inspection of data shows that the largest values of C_D for the following-wind swell were obtained after rapid changes in the wind direction (about 90°–140°). If we exclude these points, we find that at low wind speeds the drag coefficient in the presence of the opposite-wind swell is larger than in the presence of the following-wind swell (see also the discussion in Babanin and Makin 2008). A more detailed analysis of the impact of swell on the drag coefficient is outside the scope of the present study.

6 Conclusions

We presented results of field measurements of the vertical profile of the swell-induced wind-speed undulations performed at several fixed heights under different wind and swell conditions. Results are interpreted within the framework of a simplified model of the marine

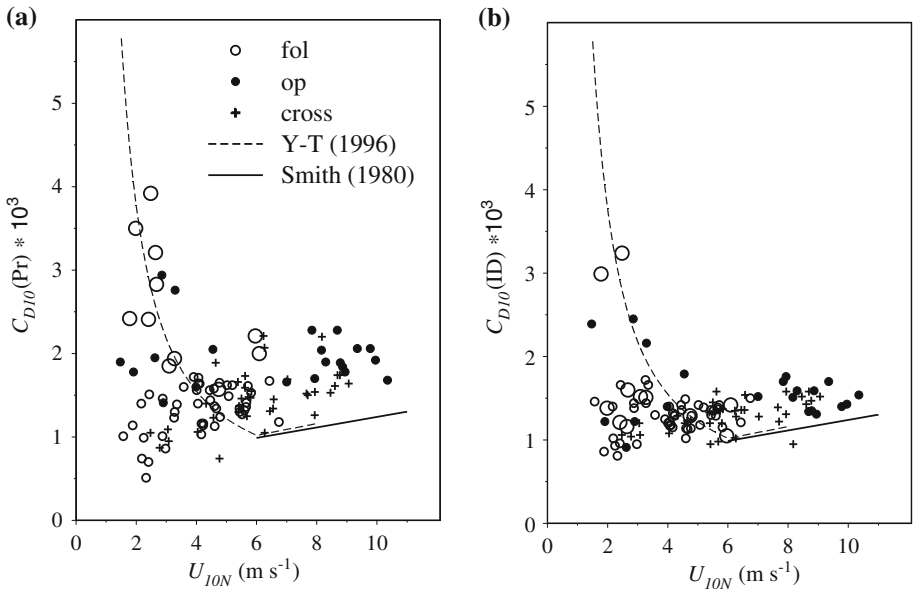

Fig. 15 The neutral drag coefficient at 10-m height estimated from the wind profile (**a**) and by the ID method (**b**) as a function of the neutral wind speed for the same data as shown in Fig. 14. The curves show the empirical relationships proposed by Yelland and Taylor (1996) (*dashed line*) and Smith (1980) (*solid line*). The large *open circles* indicate data for the following-wind swell obtained after significant change of the wind direction

atmospheric boundary layer proposed by Kudryavtsev et al. (2001) and Kudryavtsev and Makin (2004). The measurements were performed in the range of the dimensionless height from $kz \approx 0.1$ to $kz \approx 3$. According to the model, this range of heights corresponds to the outer region of the MABL, where the swell-induced undulations should exhibit properties of the inviscid shear flow. We found that the model is consistent with the measurements, and we have not revealed any remarkable deviations of the dynamics of the swell-induced undulations from the model prediction for the inviscid shear flow.

This fact presumes that the direct impact of swell on the turbulence is confined to a thin layer (with thickness less than $kz = 0.1$) adjacent to the surface, and the mean properties of the turbulence in the layer $kz > 0.1$ should be similar to the equilibrium turbulent boundary layer, in accordance with the Monin-Obukhov theory. Our data confirmed this assumption: (i) the wind-speed profile adjusted to neutral conditions has the logarithmic form; (ii) spectra of the wind-speed fluctuations in the inertial subrange correspond to the "universal" form of the Kolmogorov-type spectra; (iii) the friction velocity derived from the wind-speed profile is comparable with estimates using the inertial-dissipation method. We also obtained that at low wind conditions the surface drag coefficient in the presence of swell exhibits very large scatter. This feature is usually attributed to the impact of swell, although the detailed analysis of these data is beyond the scope of the present study.

Acknowledgements The authors are grateful to Dr. Vladimir Dulov for the opportunity to use the wave-directional spectra data. The authors are very grateful to Alexey Korovushkin, Yuri Toloknov and Alexander Bolshakov for their technical assistance in carrying the measurements. The authors would like to thank Dr. Vladimir Makin and Dr. Alex Babanin for helpful comments and discussion. The support from Norwegian

Cooperation Programme on "Research and Higher Education with Russia, 2007-2010", Project ES4303333, and ONR grant N00014-08-1-0609 is gratefully acknowledged.

References

Ardhuin F, Chapron B, Collard F (2009) Observation of swell dissipation across oceans. Geophys Res Lett 36:L06607. doi:10.1029/2008GL037030

Babanin AV, Makin VK (2008) Effects of wind trend and gustiness on the sea drag: lake George study. J Geophys Res 113:C02015. doi:10.1029/2007JC004233

Babanin AV, Soloviev YuP (1987) Parameterization of the width of angular distribution of the wind wave energy at limited fetches. Izv Atmos Ocean Phys 23:645–651

Belcher SE, Hunt JCR (1993) Turbulent shear flow over slowly moving waves. J Fluid Mech 251:109–148

Britter ML, Hunt JCR, Mumford J (1979) The distortion of turbulence by a circular cylinder. J Fluid Mech 92:269–301

Capon J (1969) High-resolution frequency-wavenumber spectrum analysis. Proc IEEE 57:1408–1418

Davidson KL, Frank AK (1973) Wave-related fluctuations in the airflow above natural waves. Phys Oceanogr 3:102–119

Donelan MA, Drennan WM, Katsaros KB (1997) The air-sea momentum flux in conditions of wind sea and swell. Phys Oceanogr 27:2087–2098

Drennan WM, Kahma KK, Donelan MA (1999) On momentum flux and velocity spectra over waves. Boundary-Layer Meteorol 92:489–515

Dupuis H, Guerin C, Hauzer D, Weill A, Nacass P, Drennan WM, Closhé S, Graber HC (2003) Impact of the flow distortion corrections on turbulent fluxes estimated by the inertial dissipation method during the FETCH experiment on R/V L'Atalante. J Geophys Res 108:8064. doi:10.1029/2001JC001075

Dyer AJ (1974) A review of flux-profile relationships. Boundary-Layer Meteorol 7:363–372

Edson JB, Fairall CW (1998) Similarity relationships in the marine atmospheric surface layer for terms in the TKE and scalar variance budgets. J Atmos Sci 55:2311–2328

Edson JB, Fairall CW, Sullivan PP et al (2007) The coupled boundary layers and air-sea transfer experiment in low winds. Bull Am Meteorol Soc 88:571–591

Garratt JR (1972) Studies of turbulence in the surface layer over water (Lough Neagh). Part II: Production and dissipation of velocity and temperature fluctuations. Q J Roy Meteorol Soc 98:642–657

Geernaert GL, Hansen F, Courtney M, Herbers T (1993) Directional attributes of the ocean surface wind stress vector. J Geophys Res 98:16571–16582

Grachev AA, Fairall CW (2001) Upward momentum transfer in the marine boundary layer. Phys Oceanogr 31:1698–1711

Grachev AA, Fairall CW, Hare JE, Edson JB, Miller SD (2003) Wind stress vector over ocean waves. Phys Oceanogr 33:2408–2429

Guo-Larsen XV, Makin VK, Smedman A-S (2003) Impact of waves on the sea drag: measurement in the Baltic Sea and a model interpretation. Glob Atmos Ocean Syst 9:97–120

Hanley KE, Belcher SE (2008) Wave-driven wind jets in the marine atmospheric boundary layer. J Atmos Sci 65:2646–2660

Harris DL (1966) The wave-driven wind. J Atmos Sci 23:688–693

Hristov TS, Miller SD, Friehe CA (2003) Dynamical coupling of wind and ocean waves through wave-induced air flow. Nature 422:55–58

Hsu CT, Hsu Y (1983) On the structure of turbulent flow over a progressive water wave: theory and experiment in a transformed, wave-following coordinate system. Part 2. J Fluid Mech 131:123–153

Jenkins GM, Watts DG (1972) Spectral analysis and its applications. Part 2, Russian edn. Mir Publishers, USSR, 287 pp

Kaimal JC, Wyngaard JC, Izumi Y, Coté OR (1972) Spectral characteristics of surface-layer turbulence. Q J Roy Meteorol Soc 98:563–589

Kitaigorodskii SA (1970) The physics of atmosphere and ocean interaction. Gidrometeoizdat, USSR, Leningrad, 284 pp

Kondo J, Fujinava Y, Naito G (1972) Wave-induced wind fluctuation over the sea. J Fluid Mech 51(part 4):751–771

Kudryavtsev VN, Makin VK (2004) Impact of swell on the marine atmospheric boundary layer. Phys Oceanogr 34:934–949

Kudryavtsev VN, Makin VK, Meirink JF (2001) Simplified model of the air flow above waves. Boundary-Layer Meteorol 100:63–90

Large WG, Pond S (1981) Open ocean momentum flux measurements in moderate to strong winds. Phys Oceanogr 11:324–336
Mastenbroek C, Makin VK, Garat MH, Giovanangeli JP (1996) Experimental evidence of the rapid distortion of turbulence in the air flow over water waves. J Fluid Mech 318:273–302
Miles JW (1957) On the generation of surface waves by shear flow. J Fluid Mech 3:185–204
Miller SD (1999) The structure of turbulent and wave-induced wind fields over open-ocean waves. PhD thesis, University of California, Irvine, 221 pp
Moat BI, Yelland MJ, Pascal RW (2006) Quantifying the airflow distortion over merchant ships. Part 1: Validation of a CFD model. J Atmos Oceanic Technol 23:341–350
Pan J, Wang DW, Hwang PA (2005) A study of wave effects on wind stress over the ocean in a fetch-limited case. J Geophys Res 110:C02020. doi:10.1029/2003JC002258
Paulson CA (1970) Representation of wind speed and temperature profiles in the unstable atmospheric surface layer. J Appl Meteorol 9:857–861
Rieder KF, Smith JA, Weller RA (1994) Observed directional characteristics of the wind, wind stress and surface waves on the open ocean. J Geophys Res 99:22589–22596
Rutgersson A, Smedman AS, Högström U (2001) Use of conventional stability parameters during swell. J Geophys Res 106:21117–21134
Smedman A-S, Högström U, Bergström H, Rutgersson A, Kahma KK, Pettersson H (1999) A case study of air-sea interaction during swell conditions. J Geophys Res 106:25833–25851
Smith SD (1980) Wind stress and heat flux over the ocean in gale force winds. Phys Oceanogr 10:709–726
Soloviev YuP, Ivanov VA (2007) Preliminary results of measurements of atmospheric turbulence over the sea. Phys Oceanogr 17:154–172
Soloviev YuP, Korovushkin AI, Toloknov YuN (2004) Characteristics of a cup anemometer and a procedure of measuring the wind velocity. Phys Oceanogr 14:173–186
Sullivan PP, Edson JB, Hristov T, McWilliams JC (2008) Large-eddy simulations and observations of atmospheric marine boundary layers above nonequilibrium surface waves. J Atmos Sci 65:1225–1245
Volkov YuA (1969) The spectra of velocity and temperature fluctuations in air flow above the agitated sea-surface. Izv Atmos Ocean Phys 5:723–730
Volkov YuA (1970) Turbulent flux of momentum and heat in the atmospheric surface layer over a disturbed sea-surface. Izv Atmos Ocean Phys 6:770–774
Yefimov VV, Sizov AA (1969) Experimental research of the field of wind velocity over waves. Izv Atmos Ocean Phys 5:930–942
Yelland MJ, Taylor PK (1996) Wind stress measurements from the open ocean. Phys Oceanogr 26:541–558